


Cite this: *J. Mater. Chem. A*, 2023, **11**, 20824

## Self-limiting thin film deposition of amorphous metal oxides from aprotic solvents for oxygen evolution electrocatalysis†

Rafael A. Prato M.,<sup>ab</sup> Jan Fransaer<sup>b</sup> and Xochitl Dominguez-Benetton  <sup>\*a</sup>

In the context of global energy and environmental challenges, developing efficient and sustainable methods for energy storage and conversion is essential. Amorphous thin films of nanoporous single and mixed Ni, Co, Fe metal oxides were deposited using *in situ* generated superoxide from dimethyl formamide (DMF) solutions, presenting a promising advancement in oxygen evolution reaction (OER) catalysis. The OER is a critical process in technologies such as water electrolysis for hydrogen production and metal–air batteries. The oxygen reduction reaction (ORR) was investigated in DMF containing tetrabutylammonium chloride (TBAC) and transition metal chlorides ( $\text{Co}^{2+}$ ,  $\text{Ni}^{2+}$ ,  $\text{Fe}^{2+}$ ). The ORR exhibited pseudo-reversibility in 0.1 M TBAC/DMF due to the stable superoxide–TBA complex ( $\text{TBAO}_2$ ). Diffusion coefficients for  $\text{TBAO}_2$  and dissolved oxygen in DMF were measured with a rotating ring-disk electrode (RRDE) setup, obtaining values of  $9.4 \times 10^{-10} \text{ m}^2 \text{ s}^{-1}$  and  $4.4 \times 10^{-9} \text{ m}^2 \text{ s}^{-1}$ , respectively. In the presence of metal ions, the superoxide radicals react rapidly, initiating oxidative precipitation of metal oxides. Amorphous oxide layers grow until the electrode passivation towards the ORR occurs, resulting in thin films. The as-deposited films displayed exceptional oxygen evolution reaction (OER) catalytic performance, with overpotentials and Tafel slopes as low as 330 mV ( $@10 \text{ mA cm}^{-2}$ ) and  $42 \text{ mV dec}^{-1}$  for  $\text{NiO}_x$  on glassy carbon (GC). The self-limiting deposition process was investigated on porous substrates, such as reticulated vitreous carbon (RVC), which demonstrated a 100 mV reduction in OER overpotential compared to GC at the same current density. This self-limiting electrodeposition method offers potential environmental benefits, including resource efficiency and reduced environmental impact. The charge transfer mechanism and long term stability of the films were explored, with results showing stability up to 160 h on GC/RVC and 600 h on Ni foam. This study reveals insights in the ORR in aprotic solvents with transition metals oxides and presents a simple, self-limiting electrodeposition method for amorphous metal oxides, paving the way for coating complex structures and advancing energy storage and conversion technologies.

Received 4th May 2023  
Accepted 11th September 2023

DOI: 10.1039/d3ta02647g

rsc.li/materials-a

## Introduction

As the global demand for clean and sustainable energy solutions grows, the development of efficient water splitting processes for hydrogen generation becomes increasingly important. One key component in this process is the oxygen evolution reaction (OER), which plays a crucial role in alkaline water electrolyzers and metal–air batteries.<sup>1,2</sup> The sluggish kinetics of the multi-step OER remains a limiting factor,<sup>3</sup> and overcoming energy losses, stability issues, and high costs of electrocatalysts is essential for achieving economical water splitting.<sup>3</sup> Precious metal catalysts, such as iridium or

ruthenium oxide, set the benchmark for OER overpotential reduction.<sup>4,5</sup> However, their high costs make them unsuitable for large-scale industrial applications.<sup>6</sup>

Significant research has focused on engineering transition metal oxides (or hydroxides) catalysts, such as Mn, Ni, Co, and Fe, as cost-effective alternatives to iridium oxide in OER applications.<sup>7–9</sup>

Innovative solutions are required to reconcile the excellent electrocatalytic properties of these transition metal oxides with their poor electronic conductivity.<sup>7,10</sup> Strategies include the use of conductive structures such as carbon<sup>11</sup> or graphene,<sup>12</sup> metallic supports like Ni,<sup>13</sup> and limiting catalyst thickness through thin-film techniques.<sup>14</sup> Synergistic effects between two or more can also reduce overpotential.<sup>15</sup> While crystalline oxides and hydroxides have received the bulk of the attention,<sup>8</sup> amorphous transition metal oxides are also gaining interest for OER electrocatalysis.<sup>15–17</sup> Nano-structuring and employing high aspect ratio structures and 3D electrodes offer opportunities for

<sup>a</sup>Separation and Conversion Technologies, VITO-Flemish Institute for Technological Research, Boeretang 200, 2400, Mol, Belgium. E-mail: xoch@vito.be<sup>b</sup>Dept. Materials Engineering, KU Leuven, Kasteelpark Arenberg 44 – Box 2450, 3001 Leuven, Belgium† Electronic supplementary information (ESI) available. See DOI: <https://doi.org/10.1039/d3ta02647g>

further performance optimization.<sup>18,19</sup> Electrodeposition is a suitable method for leveraging these structures.<sup>14,20</sup>

Depositing thin films of functional materials for electrochemical applications has been a staple in nanomaterial research.<sup>21</sup> Limiting film thickness minimizes ohmic losses due to the poor conductivities of the oxide films, lowers overpotentials and, ultimately, increases energy savings.<sup>10</sup> Electrodeposition is a fast, cost-effective method for creating nanostructured surfaces on conductive supports.<sup>20</sup> To exploit nanostructured or porous electrodes, deposition methods must coat as much of the surface area as possible, including the inside of pore walls in the case of porous electrodes. Self-limiting electrodeposition allows coating grow to a certain thickness on outer layers, then continue on the exposed inner substrate walls.<sup>22</sup> The underlying principle is that the coating should passivate the electrode enough for the reaction to occur, preferentially on the (more conductive) exposed substrate.<sup>20</sup> This process requires balancing film thickness with pore accessibility.<sup>23</sup> The choice of substrate and its pore structure is critical for achieving the desired equilibrium, as mass transport of the precursors to the inner pore walls must not be limiting. Thus, both deposition method and the choice of substrate are essential for achieving a successful coating. Furthermore, once the coated electrodes are polarized for the oxygen evolution reaction, rapid transport of oxygen out of the structure must be managed.

In this study, we present a cathodic electrodeposition method to produce self-limiting thin films of amorphous mixed metal oxides without the use of complex precursors. Building on the work of Vanhoutte *et al.*,<sup>20</sup> we use dimethylformamide (DMF) as an aprotic solvent to promote the 1 electron oxygen reduction to superoxide, which reacts with and deposits metals from solution as metal oxides (MO<sub>x</sub>). Due to the high reactivity of superoxide, the method results in a fast deposition process capable of uniformly precipitating mixtures of metal ions. We investigate the oxygen reduction reaction in metal-free DMF and use a quaternary ammonium ion to stabilize the superoxide radical. This increased stability enables probing diffusion coefficients, saturation concentrations, and the electrochemical behavior of the system. The method is then used to deposit Ni, Co and Fe oxide films onto flat glassy carbon electrodes for structural and electrochemical characterization. Reticulated vitreous carbon is coated to showcase the self-limiting behavior of the deposition technique. The porous structures serve as an ideal substrate for enhanced OER performance after coating. Finally, we use of Ni foam as a substrate, providing increased surface area, increased OER catalytic activity, and improved substrate-coating interfacial stability with promising results. This self-limiting electrodeposition method offers potential environmental benefits, including resource efficiency and reduced environmental impact, while advancing energy storage and conversion technologies.

## Experimental methods

### ORR study

To study the ORR, we prepared 0.1 M tetrabutyl ammonium chloride (TBAC, VWR MFCD00011635) in dimethyl formamide

(VWR *N,N*-dimethylformamide, Extra Dry  $\geq 99.8\%$ , AcroSeal™). All reactants were purchased dry, and used dry, under nitrogen or oxygen atmosphere. For the oxygen-saturated solutions, oxygen was bubbled for at least 30 minutes before each experiment. Otherwise, nitrogen was bubbled similarly, for nitrogen-saturated solutions. During the experiments the appropriate gas was introduced on top of the solutions.

A saturated calomel electrode (SCE) with a ceramic frit was used as the reference electrode, and a carbon electrode served as the anode. Prior to each experiment, the reference electrodes were calibrated *vs.* a pristine Ag/AgCl reference electrode (never used in an experiment) in a 3 M KCl solution. Calibrating the SCE against a pristine Ag/AgCl reference electrode, as done in our study, involved comparing the potential readings of the SCE to the potential readings of the Ag/AgCl electrode, both of which were immersed in the same electrolyte solution. This calibration step was undertaken to ensure the accurate reporting of the potentials in the system. Using a pristine Ag/AgCl electrode for all the experiments we conducted could have been an option for a few short-term experiments. But this was not the case for the long-term, as the Ag/AgCl electrode may face stability issues, not due to the nature of the electrode but due to the type of junction (*i.e.*, a single junction of glass). The SCE electrode was primarily chosen due to its ceramic frit. Ceramic frits are often selected for their chemical inertness and robustness in various solvent systems, including non-aqueous solvents like dimethylformamide (DMF). Glass frits might be more susceptible to interactions with certain solvents or experimental conditions. Given that your experiments are conducted in DMF, the ceramic frit in the SCE was deemed as a more compatible and stable choice under these conditions. Ceramic frits have less potential drift compared to an Ag/AgCl electrode with a glass frit. The potential stability of the SCE itself (with a ceramic frit), thus contributed to the reliability of our calibration. Plus, here are numerous studies in literature using SCE in DMF, and thus it has a well characterized behavior in this medium.

The working electrodes consisted of 3 mm diameter glassy carbon disks (EDAQ ET074-1). Cyclic voltammetries were performed using a BioLogic VMP3 potentiostat, with potential ranges from 0.0 V *vs.* SCE to  $-2.0$  V,  $1.5$  V, or  $1.0$  V *vs.* SCE as indicated, at a scan rate of  $20 \text{ mV s}^{-1}$ .

Rotating ring-disk electrode (RRDE) experiments were carried out with a WaveVortex 10 (PINE research) rotator and an E6R2 RRDE tip electrode (PINE research), featuring a 5.5 mm diameter GC disk and a platinum ring with 6.5 mm inner and 8.5 mm outer diameter, respectively. The CV-CA experiments involved a CV applied to the disk with a scan rate of  $50 \text{ mV s}^{-1}$  and a chronoamperometry (CA) at the ring at 0.0 V *vs.* SCE. Transient time experiments were executed by applying a potential at the ring of either  $-1.3$  V or 0.0 V *vs.* SCE; meanwhile, the disk was stepped from open circuit potential (OCP) to  $-1.3$  V *vs.* SCE.

The ORR study in DMF provides insights into the behavior of the oxygen reduction reaction in aprotic solvents, which is essential for understanding and optimizing the electrodeposition process of amorphous metal oxides for energy and environmental applications.



## Thin film deposition

The films of amorphous metal oxides were deposited using the same equipment as described earlier, from solutions containing 0.1 M metal chlorides ( $\text{NiCl}_2$ ,  $\text{CoCl}_2$ , and  $\text{FeCl}_2$ ) in DMF. The solutions were saturated with  $\text{O}_2$  following the same procedure as for the ORR study.

The CVs were limited to  $-1.0$  V vs. SCE, and performed between 1 and 20 times with a scan rate of  $20 \text{ mV s}^{-1}$ . The solutions were either of single metal precursors, or equimolar mixtures of 2 metals totaling 0.1 M. The concentration of the solutions was measured *via* Inductive Coupled Plasma – Optical Emission Spectroscopy (ICP-OES). The Ni foam electrodes used were cleaned *via* sonication in 3 M HCl for 15 min, followed by sonication in water, and then DMF.

By optimizing the deposition process for thin films of amorphous metal oxides, this study aimed to enhance the efficiency and sustainability of the system.

## OER catalyst evaluation

The coated electrodes were evaluated for their OER catalytic performance, by placing them in a 250 mL 1.0 M KOH solution under heavy stirring in a 3-necked flask, fitted a pH meter, a Ag/AgCl reference electrode, and a carbon cloth counter electrode.

Before all experiments, the ohmic drop was determined *via* electrochemical impedance spectroscopy (EIS) to apply an IR correction (at 85%) of the subsequent measurements. The working electrode was cycled 100 times from 0.3 V to 0.6 V vs. Ag/AgCl at a scan rate of  $20 \text{ mV s}^{-1}$ . Upon completion of the CVs, 3 Linear Scan Voltammeteries (LSVs) were applied at  $5 \text{ mV s}^{-1}$  again from OCP to 0.6 V vs. Ag/AgCl. Five more CVs were performed from  $-0.1$  V to 0 V vs. Ag/AgCl at  $10 \text{ mV s}^{-1}$ ,  $20 \text{ mV s}^{-1}$ ,  $100 \text{ mV s}^{-1}$ ,  $200 \text{ mV s}^{-1}$ , and  $500 \text{ mV s}^{-1}$ , to determine the capacitance of the films. Finally, EIS was used to probe the reaction mechanism at different overpotentials (calculated using  $1.23$  V vs. RHE as the OER onset potential) by first fixing the potential at the desired level for 5 minutes, and then starting the EIS experiments. A peak-to-peak amplitude of 10 mV was chosen, with frequencies between 200 kHz to 10 mHz.

Stability tests were performed by drawing a fixed current density and measuring the potential in a 1.0 M KOH solution under heavy stirring. The potential conversion from the reference electrode to OER overpotential was performed with the following formula:  $\eta = E(\text{vs. Ag/AgCl}) + E_{\text{REF}} + \text{pH} \cdot 0.059 - 1.233$ , where  $E(\text{vs. Ag/AgCl})$  is the potential measured for the working electrode and  $E_{\text{REF}}$  is the potential of the Ag/AgCl reference electrode used. This reference potential was calibrated prior to each experiment vs. a pristine reference electrode in a 3 M KCl solution, to account for the measured potential, reference potential, and pH.

By evaluating the OER catalytic performance, the efficiency, stability, and overall effectiveness of the developed catalysts can be determined. This information is crucial for optimizing the catalyst design and improving the performance of energy storage and conversion systems.

## Material characterization

X-Ray Diffraction (XRD). The films were deposited on flat glassy carbon plates to analyze by X-ray diffraction (XRD) in a Pan-Alytical X'Pert Pro diffractometer using a Cu K $\alpha$  radiation source. Measurements were performed with a spinner at 40 mA–40 kV spending 4 s per step with a step size of  $0.04^\circ 2\theta$  in the  $10$ – $110^\circ 2\theta$  range. The analysis was performed using High-Score Plus software. Additional XRD characterization was performed using an in-plane attachment to measure the grazing incidence diffraction on the films.

Scanning Electron Microscopy (SEM). Micrographs of the films were taken with a FEI Nova NanoSEM 450. SEM micrographs presented were taken with secondary electrons and an acceleration voltage of 5.00 kV. The films for microscopy were either deposited on the flat glassy carbon plates or on the foam electrodes.

## Results and discussion

### Oxygen reduction in DMF

Investigating the ORR is of critical importance in addressing the energy-environment nexus and tackling broader energy and environmental challenges. A deeper understanding of the ORR process can pave the way for advancements in energy storage and conversion technologies, such as water electrolysis for hydrogen production and metal–air batteries, as these technologies hold great potential in promoting a sustainable energy landscape and mitigating climate change by reducing our dependence on fossil fuels and lowering greenhouse gas emissions.

Optimizing the ORR process in DMF-based electrolytes can lead to improved efficiency and performance of electrochemical devices, enabling the development of cleaner and more effective energy solutions. This, in turn, can contribute to resource efficiency and reduced environmental impact, aligning with global goals for sustainable development and environmental protection. In this study, the oxygen reduction reaction (reaction (1)) was thoroughly investigated in different DMF-based electrolytes using a glassy carbon electrode to understand the fundamental electrochemical behavior of these systems. An initial assessment of the undisturbed ORR and its reversibility was carried out using 0.1 M Tetrabutyl Ammonium Chloride (TBAC) in DMF electrolyte.

CVs of an oxygen saturated TBAC/DMF solution were obtained at scan rates of  $10 \text{ mV s}^{-1}$ ,  $100 \text{ mV s}^{-1}$ ,  $500 \text{ mV s}^{-1}$ ,  $1000 \text{ mV s}^{-1}$ , as depicted in Fig. 1a. Redox peaks for the forward and backward reaction (1) appear at  $-0.8$  V/ $-0.9$  V vs. SCE at  $10 \text{ mV s}^{-1}$ , indicating the pseudo-reversibility of the reaction due to a 100 mV shift in peak potential. The ORR in these systems commences with the 1-electron reduction of dissolved oxygen ( $\text{O}_2$ ),<sup>24</sup> followed by the re-oxidation of the superoxide radical ( $\text{O}_2^{\cdot-}$ ); however, the reaction is not completely reversible.<sup>25</sup> As superoxide radicals are unstable in DMF, leading to solvent degradation,<sup>26</sup> quaternary ammonium ions (e.g.,  $\text{TBA}^+$ ) are employed to form a complex and stabilize the species (reaction (2)).<sup>27,28</sup> The resulting  $\text{TBA}^+-\text{O}_2^{\cdot-}$  species, being much larger, impedes full reversibility in terms of mass transport. The



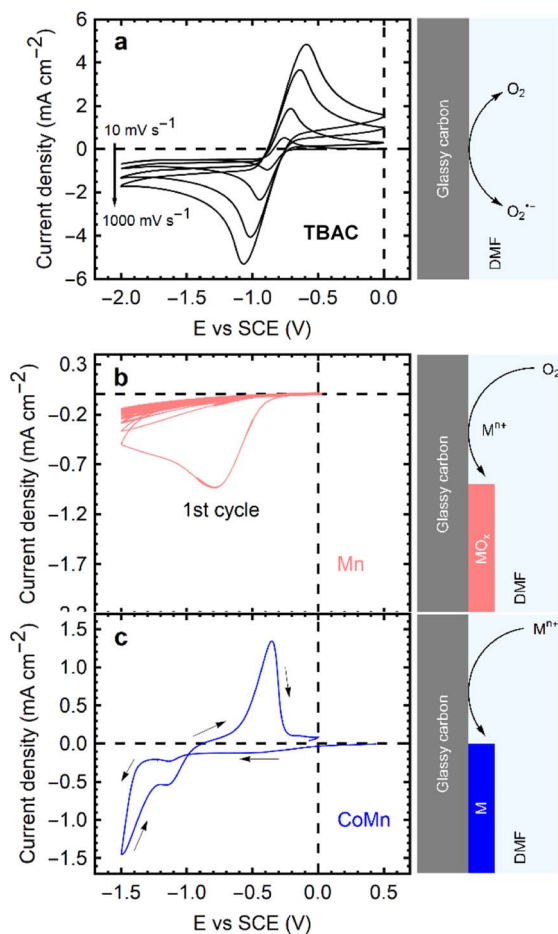
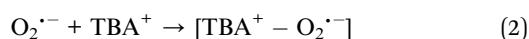


Fig. 1 Current density vs. potential cycles of a GCE in DMF with: (a) 0.1 M TBAC, saturated with oxygen, at scan rates of 10  $\text{mV s}^{-1}$ , 100  $\text{mV s}^{-1}$ , 500  $\text{mV s}^{-1}$ , 1000  $\text{mV s}^{-1}$ . (b) 0.1 M  $\text{MnCl}_2$  saturated with oxygen, at 50  $\text{mV s}^{-1}$ . (c) 0.05 M  $\text{CoCl}_2$ , 0.05 M  $\text{MnCl}_2$ , de-oxygenated, at 50  $\text{mV s}^{-1}$ . Sketches of the respective processes accompany the curves.

expected re-oxidation peaks are observed, but the charge resulting from the negative sweep is slightly larger than the reverse, suggesting the loss of radicals during the cycling time due to diffusion away from the electrode. The peak currents from the CVs in Fig. 1a are collected in Fig. S1 (see ESI†). The  $\text{TBA}^+-\text{O}_2^{\cdot-}$  itself can react with DMF and decompose the solvent at longer timescales (reaction (2)). Nonetheless, even at 10  $\text{mV s}^{-1}$  (a peak-to-peak time of 230 s), the reaction is demonstrated to be mostly reversible, attesting to the (short term) stability of the system.



To further investigate the reaction, a rotating ring-disk electrode was employed. Oxygen is reduced at the disk, where convection pushes the radicals outwards towards the ring. The stability of the  $\text{TBA}^+-\text{O}_2^{\cdot-}$  enables its transport to the ring,

facilitating oxidation back to  $\text{O}_2$ . The ring current was calibrated using the ferri/ferro redox couple to measure the collection efficiency of the electrode (38%), arising from the electrode's geometry.

Fig. 2a shows CVs on the disk at 50  $\text{mV s}^{-1}$  for the reduction of oxygen, and the resulting ring currents (polarized at 0.0 V vs. SCE) to oxidize the superoxide. At rotation speeds below 200 rpm, an oxidation peak is observed on the reverse sweep at the disk, indicating the presence of residual  $\text{TBA}^+-\text{O}_2^{\cdot-}$  at the surface of the disk electrode. The convection at low rotation speeds is insufficient to completely remove the species from the disk surface before the reverse sweep. To examine these diffusion rates and determine the diffusion coefficients of both species, transient experiments were conducted on the RRDE. Two experiments were designed to measure the diffusion coefficients of  $\text{O}_2$  and  $\text{TBA}^+-\text{O}_2^{\cdot-}$ . First, the ring is polarized at 0.0 V vs. SCE, a potential at which  $\text{TBA}^+-\text{O}_2^{\cdot-}$  is oxidized, representing a key advancement in the understanding of the

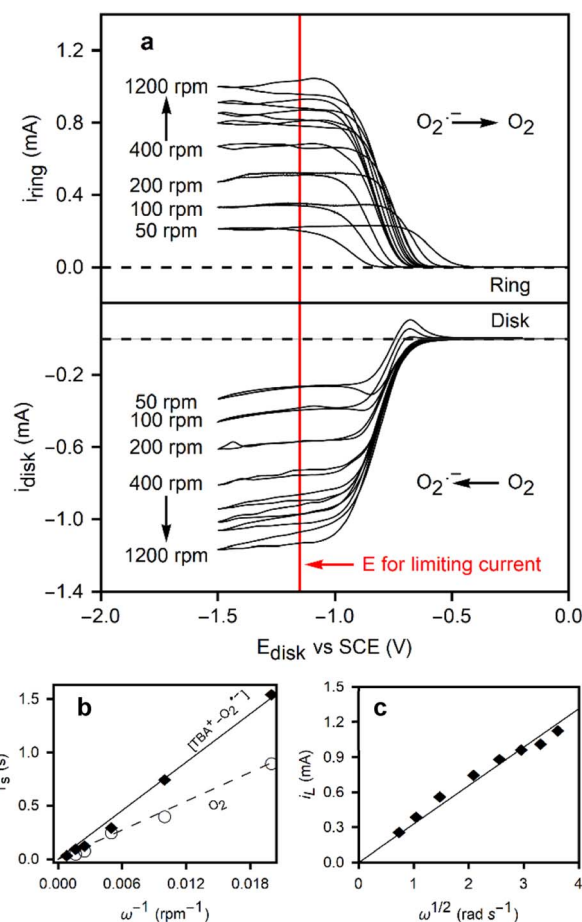


Fig. 2 (a) Rotating ring disk electrode experiment with a cyclic voltammetry applied to the disk electrode with a 50  $\text{mV s}^{-1}$  at various rotating speeds, and a chronoamperometry with 0.0 V vs. SCE at the ring, in a 0.1 M TBACl solution saturated with oxygen. The red line denotes the potential at which transient time experiments are performed and the limiting current is taken. (b) Transient time of oxygen/superoxide during the ORR in the RRDE setup at different rotation speeds. (c) Levich plot of the limiting currents as a function of rotation speed. The solid line is the fit from eqn (5).



electrochemical behavior of this species. A step in potential brings the disk to  $-1.2$  V vs. SCE, performed at different rotation speeds, allowing for an in-depth study of the reaction kinetics. The current onset on the ring is used to determine the time required for the  $\text{TBA}^+-\text{O}_2^{\cdot-}$  to reach the ring ( $T_s$ ). This transient time is given by eqn (3).

$$T_s = K \left( \frac{\nu}{D} \right)^{\frac{1}{3}} \omega^{-1} \quad (3)$$

Here,  $K$  represents the electrode geometric constant ( $43.1 \log_{10}(r_2/r_1)^{2/3}$ ) where  $r_2$  is the inner ring radius (m),  $r_1$  is the disk radius (m),  $\omega$  is the rotation speed (rpm),  $D$  is the diffusion coefficient ( $\text{m}^2 \text{s}^{-1}$ ), and  $\nu$  is the kinematic viscosity ( $9.74 \times 10^{-7} \text{ m}^2 \text{s}^{-1}$  at  $20^\circ \text{C}$ ). This approach enables a more precise determination of the diffusion coefficient, a crucial parameter for understanding the electrochemical behavior of the  $\text{TBA}^+-\text{O}_2^{\cdot-}$  species. The same experiment was repeated for the  $\text{O}_2$  diffusion coefficient, but in this case, the ring potential was set to  $-1.2$  V vs. SCE. The relationship between the transient times and the inverse of the rotation speed can be used to calculate the diffusion coefficients, as shown in Fig. 2b. The larger  $\text{TBA}^+-\text{O}_2^{\cdot-}$  species yielded a diffusion coefficient 4.7 times smaller than that of  $\text{O}_2$  in DMF,  $9.43 \pm 0.02 \times 10^{-10} \text{ m}^2 \text{s}^{-1}$  and  $4.80 \pm 0.01 \times 10^{-9} \text{ m}^2 \text{s}^{-1}$ , respectively. This results in very close agreement with Vasudevan's measurement of  $D_{\text{O}_2} = 4.89 \times 10^{-9} \text{ m}^2 \text{s}^{-1}$ , as well as others in the scientific literature.<sup>27–29</sup> Details of the transient time measurements are provided in Fig. S3.†

Given the diffusion coefficient, the limiting currents in the RRDE experiments in Fig. 2c can be used to calculate the oxygen concentration, a critical parameter for understanding the electrochemical behavior of the system. The Levich eqn (4) is as follows:

$$I_L = 0.620nFAD^{2/3}\nu^{-1/6}C\omega^{1/2} \quad (4)$$

$I_L$  (A) refers to the limiting current measured in the RRDE experiments in Fig. 2a at the potential marked by the red line.  $A$  is the surface area ( $\text{m}^2$ ),  $F$  is Faraday's constant ( $\text{C mol}^{-1}$ ),  $n$  is the number of moles transferred in the electrochemical reaction (1), and  $C$  is the oxygen concentration ( $\text{mol m}^{-3}$ ). Using the diffusion coefficient calculated *via* the transient time experiments, an oxygen concentration of 2.75 mM results, representing a reliable determination of oxygen concentration in DMF.

The Randles–Sevcik equation (eqn (5)), and the voltammetry data in Fig. S1,† can be used to corroborate the diffusion coefficients obtained from the RRDE experiments:

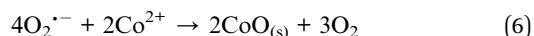
$$j_p = 0.4463 \left( \frac{F^3}{RT} \right)^{1/2} n^{3/2} D^{1/2} C \nu^{1/2} \quad (5)$$

where  $j_p$  denotes the peak current density ( $\text{A m}^{-2}$ ),  $R$  is the ideal gas constant ( $\text{J mol}^{-1} \text{K}^{-1}$ ),  $T$  is temperature (K), and  $\nu$  is the scan rate ( $\text{V s}^{-1}$ ). The data from Fig. 1a yielded an oxygen concentration of 2.80 mM in DMF. The close agreement between values (2.75 mM vs. 2.80 mM) underscores the robustness of the various methods employed for determining

oxygen concentration and diffusion coefficients. This consistency contributes to the scientific impact of our study, as it demonstrates an effective combination of techniques for more accurate measurements.

Besides the  $\text{O}_2 + \text{TBAC}/\text{DMF}$  electrolyte, two alternative electrolytes were examined, as shown in Fig. 1b and c. Metal chlorides (0.1 M) were prepared in DMF, with oxygen bubbled into the solution to saturation, for Fig. 1b, and nitrogen bubbled for Fig. 1c eliminate oxygen from the solution.

In presence of transition metals and oxygen, the ORR peak appears as in the TBAC electrolyte, albeit with a significantly lower peak current density and no reversibility. Starting from the second cycle, no distinct reduction peak is discernible; instead, a diminished cathodic current appears, which decreases in magnitude with every subsequent peak (Fig. 1b). This decrease in maximum lessens as the cycle number increases, eventually until it pseudo-stabilizing (with less than a 2% change) by the 20th cycle. Cui *et al.* explored the superoxide radical reaction with divalent cobalt ions in solution *via* disproportionation:<sup>30</sup>



As the superoxide reacts with the metal ions, no oxidation current is seen on the reverse sweeps (Fig. 1b). The metal oxides deposit as thin films and passivate the electrode,<sup>20,30</sup> inhibiting further oxygen reduction and thus limiting the ORR in each subsequent sweep. When both the metal chloride and TBAC are used in oxygen-saturated electrolytes, the effects fluctuate depending on electrolyte concentration. Fig. S2 (ESI†) demonstrates the impact of increasing metal concentration in a TBAC electrolyte. In addition to the heightened current density resulting from the increased solution conductivity, larger amounts of metal ions decrease the reversibility of the solution, even in the presence of  $\text{TBA}^+$ . The superoxide produced *via* the ORR can react with cations in solution, regardless of the presence of the  $\text{TBA}^+$  complex (reaction (7)).



In the absence of oxygen, CVs such as the one in Fig. 1c are obtained. No reduction peaks are observed between 0.0 and  $-1.0$  V vs. SCE. At more negative potentials, direct metal electrodeposition begins. Conductive metallic films, evidenced by the stronger currents in the return sweep, are deposited on the electrode at reducing potentials. The metal films are oxidized at  $-0.5$  V vs. SCE. Consequently, to circumvent electrodeposition of metallic films, all subsequent deposition experiments are performed in a potential range of 0.0 V to  $-1.0$  V vs. SCE in oxygen saturated solutions.

Beyond the purposes of the present study, these findings serve as a stepping stone for gaining deeper understanding of the limiting factors in ORR, developing new approaches to overcome these limitations, and designing improved electrolytes and electrodes for electrochemical applications with the potential to significantly improve their performance.



### NMCF single and mixed oxide films as OER electrocatalysts

The general scheme for depositing single and mixed metal oxide films *via* the ORR is shown in Fig. 1b. Fig. 3 showcases the deposition cycles for each metal ion and their binary mixes. The nanoSEM image in Fig. S4 (see ESI†) reveals the morphology of a  $\text{CoO}_x$  film, which consists of rough nanostructures forming a densely packed film that covers the entire substrate. These oxide films exhibit amorphous characteristics (see Fig. S5 in ESI†), a consequence of the rapid deposition process, insufficient thermal energy, and the inhomogeneous formation method, which are expected to result in low crystallinity.<sup>20</sup> The same deposition behavior is observed for all tested electrolytes, except for those containing  $\text{FeCl}_2$  (Fig. 3).

Oxygen dissolution in the saturation step prior to electrochemical experiments oxidizes  $\text{Fe(II)}$  to  $\text{Fe(III)}$ , altering the color of the solution from yellow to brown. Upon starting the CV, a reduction peak appears at 0.0 V *vs.* SCE for the reverse reaction ( $\text{Fe(III)} \rightarrow \text{Fe(II)}$ ), followed by the expected oxygen reduction peak. In this case, a larger reduction current persists throughout the CVs for the reduction of  $\text{Fe}^{3+}$ . For mixed metal solutions containing  $\text{FeCl}_2$ , the magnitude of the current in the CVs lies between that of each single metal deposition, with the  $\text{Fe(III)}$  reduction peak still visible. The presence of metal ions in

all cases reduces the overpotential for the ORR in the initial deposition cycle relative to that in the TBAC electrolytes.

A benchmark test of these metal oxide films was performed to identify trends in terms of OER electrocatalytic activity and to compare this technique with similar existing methods in scientific literature. The most common benchmark parameters include overpotential at set current densities and Tafel slopes. Fig. 4b presents the polarization curves of the films before and after electrochemical conditioning, along with the extracted Tafel slopes, and the conditioning process itself. The first polarization curve (Fig. 4a) for  $\text{FeO}_x$  shows no significant pre-catalytic current, indicating full  $\text{Fe(III)}$  content, which is expected given that the solubility of oxygen in the  $\text{Fe(II)/DMF}$  solution is sufficient to oxidize all iron ions.  $\text{CoO}_x$  exhibits a small oxidative peak at +1.08 V *vs.* RHE during the first polarization curve, attributed to the  $\text{Co(II)}$  to  $\text{Co(III)}$  oxidation

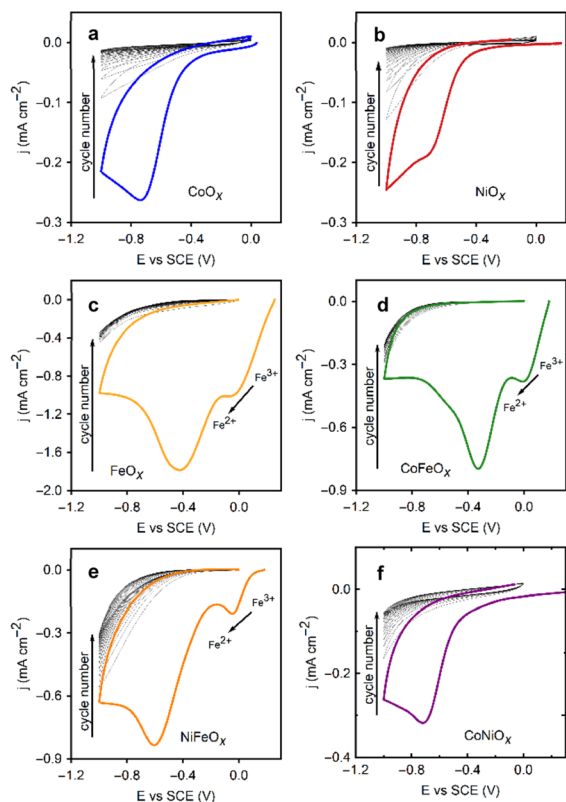


Fig. 3 Cyclic voltammograms at  $20 \text{ mV s}^{-1}$  of the deposition of the single (Ni, Co, Fe) and mixed (CoFe, NiFe, CoNi) metal oxides over 20 cycles. Potential regions for the electrochemical reactions discussed are noted. The cycle number increases from each initial cycle highlighted, to the subsequent cycles trending towards 0 current. (a) Co. (b) Ni. (c) Fe. (d) CoFe. (e) NiFe. (f) CoNi.

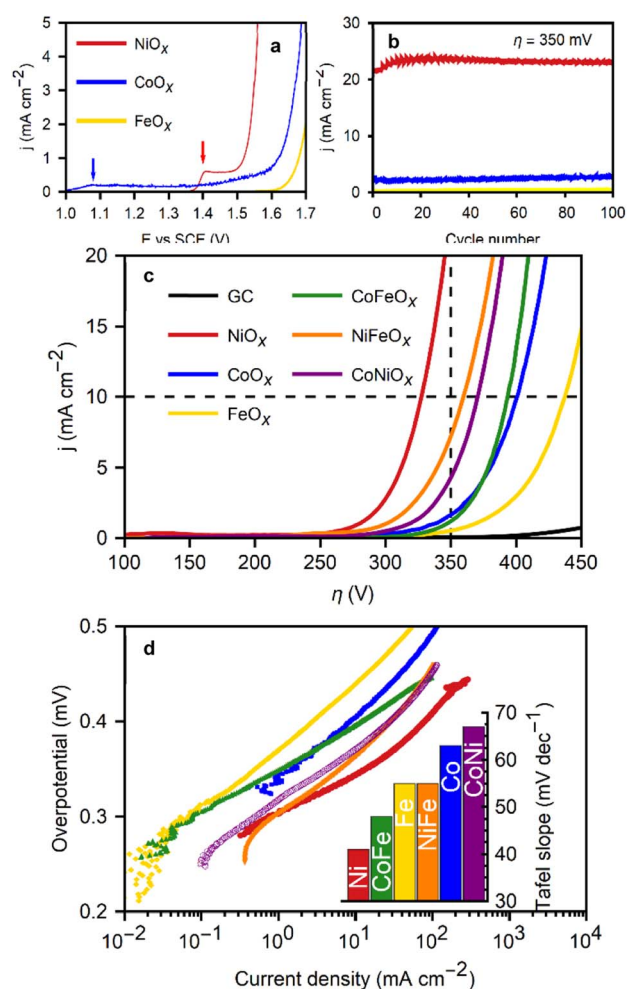


Fig. 4 Electrocatalytic response from metal oxide films on glassy carbon for the OER in 1 M KOH. (a) First polarization curves for Fe, Co, and Ni oxide films. (b) Current density at an overpotential of 350 mV during 100 conditioning cycles for Fe, Co, and Ni oxides. (c) Polarization curves for all oxides studied and the bare glassy carbon substrate, relevant conditions of  $10 \text{ mA cm}^{-2}$  and 350 mV of overpotential are noted (d) Tafel plots with the slopes as an inset of the metal oxide films OER activity.

prior to the onset of the OER at +1.35 V vs. RHE.<sup>16</sup> The low peak current ( $<0.2 \text{ mA cm}^{-2}$ ) suggests that only a small amount of the initial Co(II) remains after the deposition. On the other hand,  $\text{NiO}_x$  films display a larger oxidation current peak ( $0.6 \text{ mA cm}^{-2}$ ) at +1.46 V vs. RHE, coinciding with the OER onset. The peak potential aligns with the expected value for the oxidation of  $\text{Ni(II)(OH)}_2$  to  $\text{Ni(III)OOH}$ , the more electrocatalytic species of Ni for the OER.<sup>10,16,31</sup> While the exact valence structure of the materials is left for further work and optimization, it can be concluded that the oxides contain a majority Fe(III) and Co(III), with partial Co(II), Ni(II), and Ni(III) content, respectively.

The as-deposited  $\text{NiO}_x$  films initially produced slightly reduced currents and larger Tafel slopes. However, their performance improved with electrochemical conditioning of the films through 100 CVs in a 1 M KOH solution. The current experienced a significant increase after the first cycle, continuing to rise for the first 20 cycles, after which the voltammetries stabilized. Subsequently, LSVs at a slower scan rate ( $5 \text{ mV s}^{-1}$ ) were performed to obtain the characteristic values of the films. Fig. 4b displays the current densities at 350 mV overpotential during the conditioning cycles for  $\text{FeO}_x$ ,  $\text{NiO}_x$ , and  $\text{CoO}_x$  films. Conditioning for Ni oxide films is known to enhance performance due to  $\text{Ni}^{2+}$  oxidation during cycling at potentials greater than 1.4 V vs. RHE, supporting the hypothesis of incomplete oxidation of the Ni ions during the deposition, with some divalent ions likely still present in the oxide. Films without Ni did not exhibit as pronounced changes during conditioning.

A clear activity trend is seen from the data:  $\text{NiO}_x$  films exhibited the best performance ( $\eta_{10\text{mAcm}^{-2}} = 330 \text{ mV}$ ), followed by  $\text{CoO}_x$  ( $\eta_{10\text{mAcm}^{-2}} = 395 \text{ mV}$ ), and lastly  $\text{FeO}_x$  ( $\eta_{10\text{mAcm}^{-2}} = 440 \text{ mV}$ ). Depositing films from binary mixtures of Fe, Co and Ni results in an increase in overpotential for  $\text{NiFeO}_x$  ( $\eta_{10\text{mAcm}^{-2}} = 370 \text{ mV}$ ) and consistent performance to  $\text{CoFeO}_x$  ( $\eta_{10\text{mAcm}^{-2}} = 380 \text{ mV}$ ) relative to the individual metal oxides. Predictably, the  $\eta_{10\text{mAcm}^{-2}}$  of the  $\text{CoNiO}_x$  films (370 mV) falls between the overpotentials of the individual metal oxide benchmarks. A full table of overpotentials is available in Fig. S6 (see ESI†). The best performing film,  $\text{NiO}_x$ , excels in terms of both Tafel slope ( $43 \text{ mV dec}^{-1}$ ), and characteristic overpotentials ( $\eta_{1\text{mAcm}^{-2}} = 280 \text{ mV}$  and  $\eta_{10\text{mAcm}^{-2}} = 325 \text{ mV}$ ). These values rank among the lowest found in the literature for non-noble metal electrodeposited catalysts, where overpotentials ( $\eta_{10\text{mAcm}^{-2}}$ ) commonly range between 350 mV and 430 mV.<sup>4,32</sup> Crystalline nanoparticles with tailored structured such as nanosheets of layered double hydroxides can exhibit slightly better performance. Otherwise, the  $\text{NiO}_x$  films presented here favourably compare with most transition metal oxides,<sup>7–9,33,34</sup> and even iridium oxide catalysts.<sup>4,5,7,35</sup>

The area used for the current density calculation is the projected area of the glassy carbon electrodes:  $0.07 \text{ cm}^2$ . After deposition, the roughness of the films yields a larger surface, which in turn contributes to the electrochemical activity of the catalysts. The electrochemically active surface area (ECSA) was calculated using the ratio of the double-layer capacitance ( $C_{\text{dl}}$ ), measured *via* CVs in the non-faradaic region, and the specific capacitance for a smooth film ( $C_s$ ). The slope of the charge

passed *versus* the scan rate in the CVs is equal to double the  $C_{\text{dl}}$  (eqn (8)). The calculated  $C_{\text{dl}}$  can be compared with the commonly used reference value of  $0.04 \text{ mF cm}^{-2}$  for smooth oxide films in alkaline media,<sup>17,18,36,37</sup> resulting in the ECSA (eqn (9)). By dividing the ECSA by the geometric surface area, a roughness factor ( $R_f$ ) is obtained.<sup>4</sup>

$$\frac{I_a - I_c}{2} = C_{\text{dl}} \frac{dE}{dt} \quad (8)$$

$$\frac{C_{\text{dl}}}{C_s} = \text{ECSA} \quad (9)$$

The  $R_f$  ranged from 7 ( $\text{NiO}_x$ ) to 25 ( $\text{CoO}_x$ ). The ECSA (and by extension  $R_f$ ) increases with the number of deposition cycles from the first to the 5th one (Fig. S7†). These are estimates of the order of magnitude by which the real surface area multiplies the geometric one, and are generally similar to the range found in other cathodic electrodeposition methods.<sup>4</sup>

The results obtained emphasize the improved performance of electrodeposited amorphous  $\text{NiO}_x$  films as catalysts for the oxygen evolution reaction (OER). The enhancement of these catalysts' performance, reflected in their low overpotentials and Tafel slopes, demonstrates their potential as a cost-effective and environmentally friendly alternative to noble metal catalysts, such as iridium oxide. The optimization of these transition metal oxide catalysts, specifically the  $\text{NiO}_x$  films, aligns with the broader research agenda of addressing global energy and environmental challenges by contributing to the advancement of efficient, sustainable, and economically viable hydrogen production technologies.

### Characterization of the OER in $\text{NiO}_x/\text{GC}$

To elucidate the morphology and electrochemical activity of the  $\text{NiO}_x$  films, advanced electrochemical measurements were conducted. Fig. 5a presents the deposition cycles for  $\text{NiO}_x$  films and the diminishing peak current discussed in previous sections. The polarization curves for  $\text{NiO}_x$  films deposited in 1, 5, and 20 cycles (Fig. 5b) demonstrate a marked improvement in OER performance after the first deposition cycle, while the performance of the films resulting from 5 or 20 deposition cycles remains indistinguishable, suggesting a saturation effect of the electrocatalytic activity.

Electrochemical impedance spectroscopy (EIS) was performed at steady-state operation in a range of applied potentials covering the low- and high-overpotential regions in the Tafel plot of Fig. 5f, providing valuable insight into the reaction kinetics and film properties. Nyquist representations of the EIS responses of  $\text{NiO}_x$  films (Fig. 5d and e) emphasize the significance of the exchange in OER between films deposited from 1 cycle in  $\text{NiCl}_2$  ( $\text{NiO}_x1\text{C}$ ) and 5 cycles ( $\text{NiO}_x5\text{C}$ ). Nine different potentials were applied during the EIS experiments ranging from 290 mV to 390 mV in overpotential for the OER reaction.

The Nyquist plot for  $\text{NiO}_x1\text{C}$  displays a single semicircle across all potentials, between the 100 kHz to 10 mHz, consistent with a passive Ni oxide film covering the electrode (*i.e.*, the magnitude of the impedance decreases with increasing





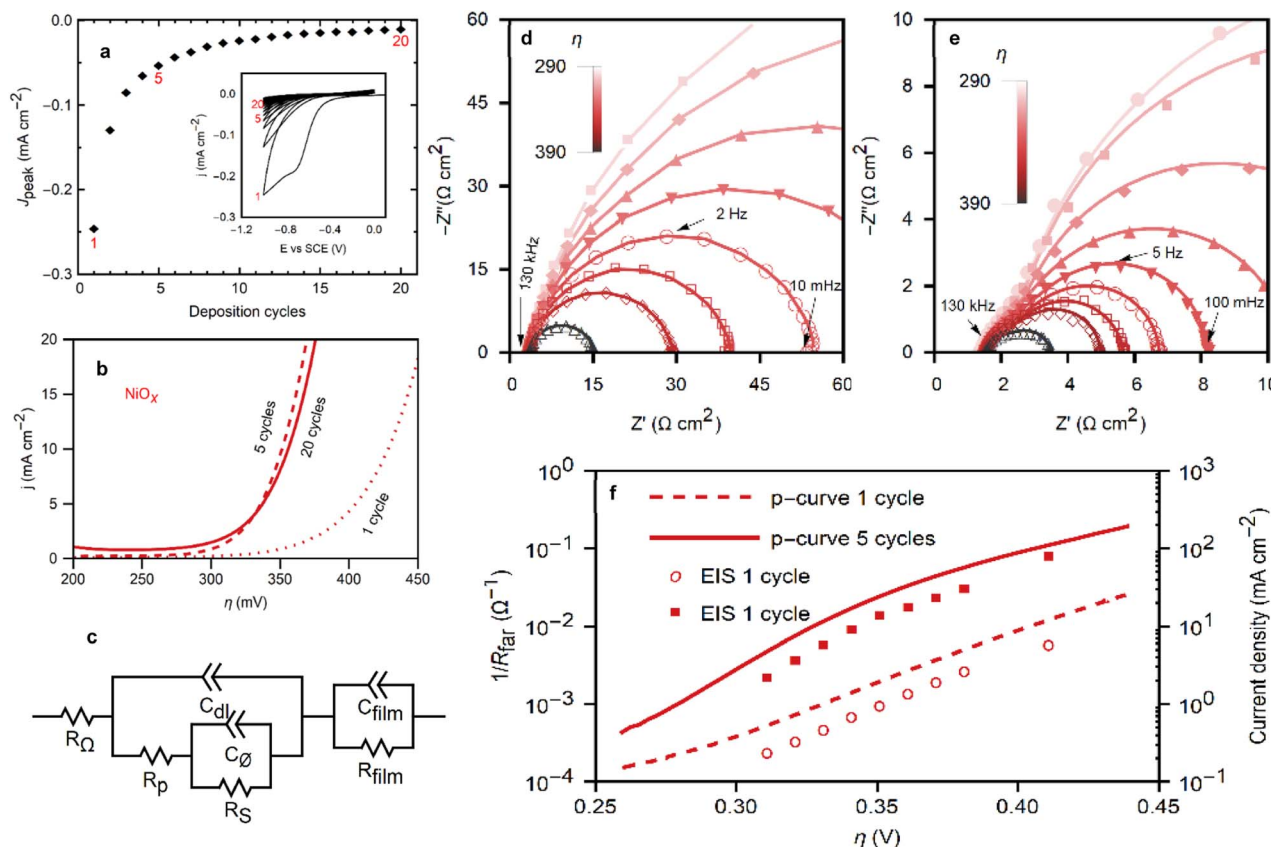


Fig. 5 (a) The peak currents of each deposition cycle from the inset are plotted with cycles 1, 5 and 20 highlighted and (inset) cyclic voltammograms at  $20 \text{ mV s}^{-1}$  of the deposition of the nickel oxides over 20 cycles. (b) Polarization curves for the OER with  $\text{NiO}_x$  films deposited from 1, 5, and 20 cycles. (c) Equivalent circuit for the impedance process adapted from Lyons *et al.*<sup>38</sup> EIS Nyquist plots of  $\text{NiO}_x$  films ((d) deposited with 1 cycle, (e) deposited with 5 cycles) on GCE in 1 M KOH at applied overpotentials ranging from 290 mV to 390 mV. (f) Tafel plots made from EIS and dc polarization data of  $\text{NiO}_x$  of films deposited from 1 and 5 cycles.

overpotential). The Bode plots in Fig. S8 (see ESI†) show more explicitly the frequency ranges for the impedance. By employing an equivalent circuit model (Fig. 5c) based on the work of Lyons *et al.*, a comprehensive analysis of the film properties and reaction kinetics can be performed, shedding light on the interfacial charge transfer processes and the impact of the catalytically active  $\text{Ni(III)}$  surface species ( $\text{NiOOH}$ ) on the OER kinetics.  $R_\Omega$  represents the uncompensated electrolyte resistance,  $R_{\text{film}}$  and  $C_{\text{film}}$  relate to the resistivity and dielectric properties of the film,  $C_{\text{dl}}$  is the double layer capacitance,  $R_p$ ,  $R_s$ , and  $C_\phi$  relate to the kinetics of the interfacial charge transfer reaction and the relaxation of the charge associated with the adsorbed intermediates.<sup>38–41</sup>

With a Tafel slope of  $60 \text{ mV dec}^{-1}$  and phase maxima in the frequency region commonly associated with the  $R_s C_\phi$  time constant, the  $\text{NiO}_x\text{1C}$  film exhibits the features of a film with kinetics that depend on the formation of the catalytically active  $\text{Ni(III)}$  surface species ( $\text{NiOOH}$ ).<sup>38,42</sup> The fitted parameters are plotted in Fig. S8 (see ESI†). Note that only  $R_s$  and  $C_\phi$  are shown for  $\text{NiO}_x\text{1C}$ . The magnitude of the impedance obscures the contributions from the other elements. The single semicircle seen in the Nyquist plot is a superposition of both time constants,  $R_s C_\phi$  and  $R_p C_{\text{dl}}$ , making the latter elements

inaccessible from these data.<sup>38</sup> Meanwhile, the dielectric properties of the film are expected to result in an impedance response that lays outside of the scanned frequency range.<sup>15,43</sup> For all capacitive elements in the impedance modelling, Constant Phase Elements (CPEs) were used instead of ideal capacitors. Frequency dispersion in CPEs ( $\alpha < 1$ ) is generally attributed to deviations from ideality, *i.e.*, roughness and inhomogeneity in the film,<sup>44</sup> as expected for a rough film (high  $R_p$ ). The CPE exponent for the  $\text{NiO}_x\text{1C}$  films ( $\alpha_{\text{CPE1}}$ ) was constant and equal to 0.87 for all applied overpotentials between 290 mV to 390 mV.

In contrast, the  $\text{NiO}_x\text{5C}$  cycle exhibits 2 distinct semicircles: a higher frequency response between  $10^3 \text{ Hz}$  and  $10^2 \text{ Hz}$  that is smaller in magnitude, and a lower frequency response with a peak between  $10^2 \text{ Hz}$  and  $10^1 \text{ Hz}$  that dominates the spectra at low overpotentials. This is indicative of an increase in the number of active sites and a more intricate interplay between the film properties and reaction kinetics. The low-frequency response for  $\text{NiO}_x\text{5C}$  is strongly dependent on the applied potential, and the high-frequency semicircle, which has a less pronounced dependency on it (Fig. 5e and S8 in ESI†), is attributed to the double-layer capacitance of the film. This element is partially masked by the  $R_s C_\phi$  response at lower





overpotentials. At a high overpotential ( $>390$  mV) the  $R_p C_{dl}$  loop becomes the larger contributor. The increased roughness factor from 6 ( $\text{NiO}_x1\text{C}$ ) to 9 ( $\text{NiO}_x5\text{C}$ ) increases the capacitive contribution, as well as the number of active sites. While the roughness increases by 50%, roughness alone cannot account for the increase in catalytic performance (Fig. 5b). At  $\eta = 350$  mV the current density increases by a factor of 10 in  $\text{NiO}_x5\text{C}$  films relative to  $\text{NiO}_x1\text{C}$  films. Furthermore, the Tafel slope decreases to  $48 \text{ mV dec}^{-1}$ . A slope of *ca.*  $40 \text{ mV dec}^{-1}$  is commonly ascribed to a rate-determining step (RDS) after the formation of the active metal intermediary. While the specific mechanism is uncertain, the RDS may involve a charge transfer process related to the oxidation of the adsorbed oxygen species, such as peroxide formation on the catalyst surface ( $\text{Ni-OH} \rightarrow \text{Ni-O}_2\text{H}_2$ ).<sup>45</sup> Thus we propose that the ORR deposition cycles not only increase the surface coverage of the electrode with the  $\text{NiO}_x$  film, but also oxidize the surface cations to their catalytically active form ( $\text{Ni(III)}$ ). As such, with a higher roughness and a more active surface, the ten-fold increase in the catalytic activity of the films after 4 ORR cycles can be explained. The Nyquist plot for  $\text{NiO}_x5\text{C}$  reflects these morphological changes, the lower faradaic resistance is comparable to the higher capacitive contribution, and is characteristic of active Ni oxide films.<sup>38</sup> Nonetheless, as shown in the previous section, some unoxidized  $\text{Ni(II)}$  sites remain on the film after 5 deposition cycles. The apparent double-layer capacitance calculated from the impedance data is larger than that obtained by cyclic voltammetry (Fig. S7†). While the voltammetry experiments were performed in a less oxidative potential range to approach a purely non-faradaic current, the potential used for the impedance experiments overlaps with that of  $\text{Ni(II)}$  oxidation (Fig. 4a). This redox reaction leads to an inflated value for  $C_{dl}$ . Rather than a true double-layer capacitance, the capacitance includes a pseudo-capacitance contribution due to a redox reaction in the film.<sup>14</sup> Recapping, this analysis provides a deeper understanding of the factors contributing to the ten-fold increase in catalytic activity observed in  $\text{NiO}_x5\text{C}$  films compared to  $\text{NiO}_x1\text{C}$  films, such as the higher roughness and the presence of a more active surface.

EIS was also employed for the Tafel analysis. A comparison with the values obtained through the polarization curves described earlier is shown in Fig. 5f. The faradaic resistance ( $R_{\text{far}}$ ) is extracted from the Nyquist plots as the low-frequency resistance minus the ohmic and film resistances ( $R_{\text{far}} = R_p + R_s$ ).<sup>42</sup> The decreased faradaic resistance from the higher concentration of active sites in  $\text{NiO}_x5\text{C}$  films *vs.*  $\text{NiO}_x1\text{C}$  films is seen in the impedance spectra. The Tafel equation relates the current with overpotential:

$$i = i_0 \exp(2.303\eta/b) \quad (10)$$

With  $b$  the Tafel slope, and  $i_0$  the exchange current density. Differentiating with respect to the overpotential

$$\frac{di}{d\eta} = \frac{2.303i_0}{b} \exp(2.303\eta/b) \quad (11)$$

Substituting  $di/d\eta$  with  $1/R_{\text{far}}$ , and taking the logarithm yields a form of the Tafel equation:<sup>40</sup>

$$\log\left(\frac{1}{R_{\text{far}}}\right) = \frac{E}{b} + \log\left(\frac{2.303i_0}{b}\right) \quad (12)$$

The results from the Tafel analysis concur with the values obtained through standard polarization curves. EIS Tafel slopes yielded  $48 \text{ mV dec}^{-1}$  and  $74 \text{ mV dec}^{-1}$ , respectively, for the low and high overpotential regions. These values are in close agreement with the  $48 \text{ mV dec}^{-1}$  and  $82 \text{ mV dec}^{-1}$  obtained from direct polarization curves for the 5 cycle film. For  $\text{NiO}_x1\text{C}$ , a single Tafel slope is observed at  $65 \text{ mV dec}^{-1}$  with both methods. The higher Tafel slope at higher overpotentials is attributed to the formation and detachment of oxygen bubbles from the active sites at high currents. The absence of two slopes observed for the  $\text{NiO}_x1\text{C}$  is attributed to the lower current densities over the analyzed range. Even at the highest overpotentials, the resulting current lies below that of the potential inflection point for  $\text{NiO}_x(5\text{C})$ . Not enough current is drawn so as to shift the kinetics of the process.

This advanced morphological and electrochemical analysis provides a more convincing and insightful understanding of the improved OER performance observed in  $\text{NiO}_x$  films.

### High current OER through porous substrates

To further explore the capabilities of the film growth method and address the needs of industrial applications, which require higher current densities than those achieved on flat substrates,<sup>15,46</sup> reticulated vitreous carbon (RVC) electrodes were utilized. The geometric surface area of the glassy carbon disks is limiting to the mass loading of the films. Microporous RVC (24 pores per cm,  $\sim 250 \mu\text{m}$  pore diameter, 2.5 mm thick) has the same electrochemical behaviour as glassy carbon, while offering a larger surface area for coating. In this way, the electrocatalytic properties of the films can be studied on 3D substrates without the interference of the substrate itself during the OER. The film deposition procedure remained consistent: ORR *via* CVs between 0.0 and  $-1.0 \text{ V vs. SCE}$  in the presence of metal chlorides in DMF. However, more deposition cycles were employed for the RVC foams to ensure total surface coverage, as the diffusion of oxygen through the pores into the inner structure of the foam slows down the deposition process. Thirty cycles were applied in this case. The self-limiting nature of the method allows for the use of more deposition cycles to coat the foam over a longer period of time, without risking clogging the pores with thick layers of material.

Fig. 6 presents the micrographs of uncoated-RVC (a), alongside progressively higher magnifications of the Co oxide coated RVC (b–d). The conformal, full-coverage, coating is shown. The carbon foam is covered homogeneously, including the inner foam walls. The self-limiting nature of the technique allows for the coating to continue onto unexposed inner walls instead of covering only the outside structure.

The increased surface area enables a larger current output during the OER, resulting in a significantly larger current



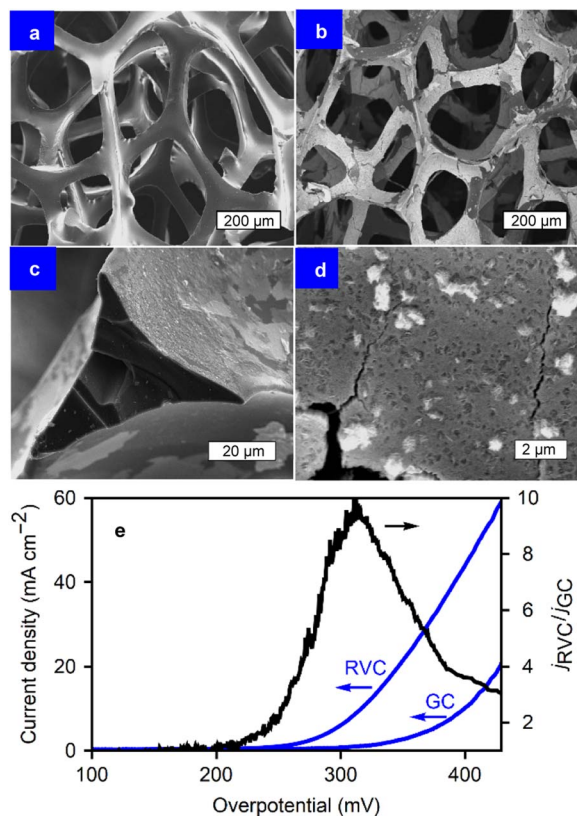


Fig. 6 SEM images of RVC electrodes (un-)coated with  $\text{CoO}_x$ . (a) Pristine RVC. (b–d) Progressively higher magnification of  $\text{CoO}_x$  films on RVC after 30 deposition cycles and electrochemical conditioning. (c) Cross section of the  $\text{CoO}_x$  films on RVC.

density than that of flat substrates (*e.g.*, GC) when considering the projected surface area. The method from Friedrich *et al.* was used to estimate the specific surface area per unit volume ( $A_s = 40 \text{ cm}^{-1}$ ),<sup>47</sup> taking into account the RVC strut dimensions from the SEM images and a density of  $0.05 \text{ g cm}^{-3}$  with 24 pores per cm. With a known  $A_s$ , the ratio of real surface area to the projected one was calculated to be 10 for this specific RVC sample. Fig. 6e displays the polarization curves for the OER performed on  $\text{CoO}_x$  for both RVC and GC, where the current increases considerably above an overpotential of 200 mV. This is likely due to a combination of the capacitive and faradaic contributions, amplifying that of the  $\text{CoO}_x/\text{GC}$  by a factor of up to 10 at  $\eta = 300 \text{ mV}$ . This represents an 85 mV decrease in overpotential at  $10 \text{ mA cm}^{-2}$  ( $\eta_{10}$ ), from 401 mV for  $\text{CoO}_x/\text{GC}$  to 316 mV for  $\text{CoO}_x/\text{RVC}$ . Such a significant decrease in  $\eta$  is in agreement with the expected surface area ratio of 10, and highlights the advantages of a porous substrate and the coating method's ability to exploit those advantages. The increased number of deposition cycles were sufficient to overcome mass transport limitations inside the porosity during coating. The ECSA of  $5.9 \text{ mF cm}^{-2}$  is 6 to 20 times higher than that of  $\text{CoO}_x$  films on glassy carbon, depending on the deposition cycles applied. Nonetheless, at high current densities, bubble formation and transport limitations become problematic. Due to the pore size, bubbles can become trapped inside the structure,

impeding further reaction at the covered sites. Consequently, the current density ratio ( $j_{\text{RVC}}/j_{\text{GC}}$ ) falls to approximately 3 for a  $j_{\text{RVC}} > 60 \text{ mA cm}^{-2}$ . If only the projected surface area on the front and back of the RVC electrodes were active, the value of  $j_{\text{RVC}}/j_{\text{GC}}$  should approach 2. With the sides of the material also being active, as well as a (diminished) contribution from the porosity,  $j_{\text{RVC}}/j_{\text{GC}}$  remains above 2 for these current densities.

It is important to note that, similar to coated GC electrodes, the metal-oxide/RVC also eventually fails during constant anodic polarization (OER). Fig. 7 shows the chronopotentiometry, demonstrating the stability of the film during 1 week of operation. After 170 hours, the catalysts begin a slow failure process. The micrographs in Fig. 7 reveal the morphology of the material before and after operation. While the initial state exhibits a mostly covered RVC substrate, during failure, the electrocatalytic oxide film is partially removed from the substrate. This delamination process is thought to be due to the poor adhesion between the glassy carbon and the metal oxides. The formation of bubbles damages the films during operation. The stability during the first 160 hours of operation, followed by a delamination process, underscores the necessity to examine catalyst stability longer than values commonly found in literature, such as 1 h, 24 h, or 100 cycles. Another contributing factor can be damage to the carbon support itself during prolonged testing.

This study provides valuable insights into the benefits of using porous substrates and serves as a basis for future research

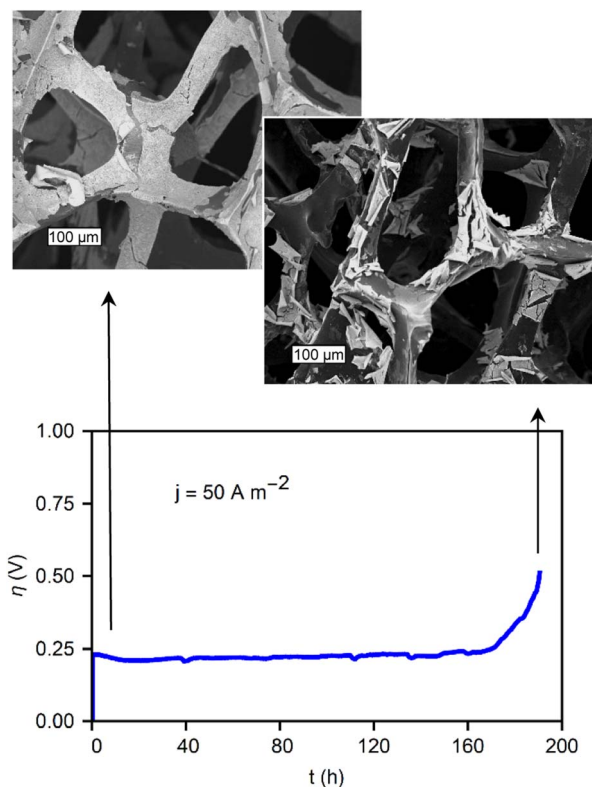


Fig. 7 CP showing the stability of a  $\text{CoO}_x/\text{RVC}$  film under a current of  $50 \text{ A m}^{-2}$  with micrographs of the material at its initial state, and after failure. The scale bars are  $100 \mu\text{m}$ .



focused on enhancing the long-term stability and performance of metal-oxide/RVC systems for industrial applications.

### Stability through better interfacial film/substrate contact

The deposition procedure was also applied to Ni-foam (NF), leveraging the porous structure to exploit the self-limiting nature of the coating method, as observed with the RVC electrodes. Additionally, NF offers superior OER electrocatalytic activity, high conductivity, and a metal/metal oxide interface.<sup>13,48</sup> The metal oxide deposition exhibits similar diminishing current densities across the subsequent deposition cycles, as observed with the GC electrode. Fig. S9 (see ESI†) presents the ORR in TBAC/DMF and  $\text{CoCl}_2 + \text{FeCl}_2/\text{DMF}$ , indicating that, unlike carbon supports, the nickel electrode can oxidize by reacting with superoxide, even in the presence of  $\text{TBA}^+$ . This reactivity leads to a loss of reversibility in the absence of metal ions in solution. Consequently, both the surface nickel and metal ions in solution can be oxidized, forming mixed-metal structures coating the metallic foam.

The SEM images in Fig. 8 display the structure of the foam at different magnifications, revealing a uniform, thin, rough surface covering the structure. EDS images in Fig. 6 highlight the foam coated with  $\text{NiCoFeO}_x$  after 20 deposition cycles in a  $\text{CoCl}_2$  and  $\text{FeCl}_2$  bath. Fig. S9 (see ESI†) provides SEM images of the TBAC cycled foam. The metals can be seen coating the entire structure. XRD traces of the coated foam, as shown in Fig. S9 (ESI†), are primarily composed of sharp reflections of metallic Ni, with small peaks of NiO and an amorphous component from the deposited metal oxide.

As the amorphous films deposited on carbon exhibited similar electrochemical behavior, the same electrochemical testing protocol was used for the foam electrodes. In Fig. S10 (ESI†) displays the CVs between 0.1 V and 0.5 V vs. SCE, demonstrating the pseudo-capacitance on the films.  $\text{CoO}_x$  films on GC were previously found to possess up to 3 times the capacitance of the other films tested. The same trend is observed on the nickel foams:  $\text{CoO}_x/\text{NF}$  exhibits significantly higher capacitance than the rest of the samples, all producing comparable CVs. The redox peak potentials shift with the addition of Fe and Co over the bare nickel foam, but the capacitance is similar overall.

The electrocatalytic performance of the films was evaluated after 100 cycles in the shown potential range. The resulting polarization curves (Fig. 8) indicate significant improvement in NF. Fe ( $\eta_{100\text{mAcm}^{-2}} = 380$  mV), Co ( $\eta_{100\text{mAcm}^{-2}} = 365$  mV), and CoFe ( $\eta_{100\text{mAcm}^{-2}} = 355$  mV) all produce similar current densities at the scanned potentials. As oxide growth occurs on a Ni substrate, all surfaces contain a mixture of Ni and the respective metals present in the deposition bath. The TBAC cycled nickel foam ( $\eta_{100\text{mAcm}^{-2}} = 400$  mV), denoted as  $\text{NiO}_x/\text{NF}$ , exhibited a substantial increase over the pristine NF ( $\eta_{100\text{mAcm}^{-2}} > 400$  mV), albeit with lower performance than the deposited oxide films. Since all the oxides deposited on nickel foam result in binary or ternary metal oxide mixes due to the oxidation of the foam itself, similar OER performance is expected with  $\text{FeO}_x$  as

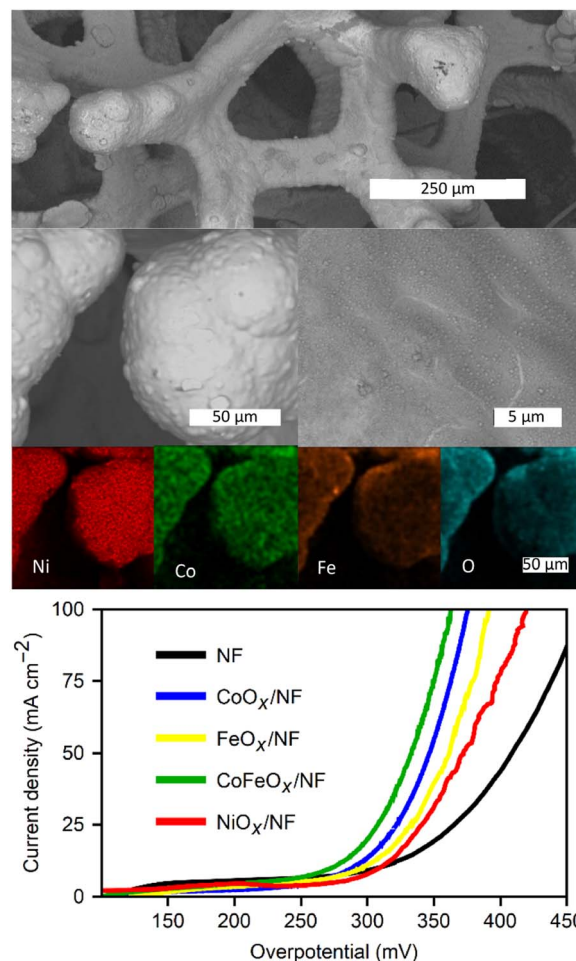


Fig. 8 SEM images from backscattered electrons of nickel foam first cycled 20 times in DMF solutions of  $\text{CoCl}_2 + \text{FeCl}_2$  and then cycled 20 times in 1.0 M  $\text{KOH}/\text{H}_2\text{O}$  for the OER tests. EDS elemental mapping of the constituent metals, and oxygen. Bottom: polarization mapping curves in 1.0 M  $\text{KOH}$  for the different oxide films.

the least effective performer and  $\text{CoFeO}_x/\text{NiO}_x/\text{Ni}$  ( $\text{CoFeO}_x/\text{NF}$ ) as the best.

The improved performance of the NF when cycled in TBAC is noteworthy. The oxidized foam (*via* ORR/superoxide) performed significantly better than bare Ni foam, and only slightly worse than the rest of the deposited films. Simply applying ORR cycles as pre-treatment to the electrode significantly improves its performance. This treatment paves the way for an even simpler activation of the foam for OER applications if these overpotentials are sufficient. Remarkably, all deposited films perform well compared to the state of the art electrocatalyst of similar composition.<sup>9,11,12,19,34</sup> Table S1 (ESI†) presents a collection of benchmarks from literature, better situating the performance of the materials presented here.

After conditioning, the  $\text{CoO}_x/\text{NF}$  was polarized at  $10 \text{ mA cm}^{-2}$  to test stability and potential evolution (Fig. 9). Over three days of polarization, the overpotential decreased. At this point ("2") new polarization curves were performed. Fig. 9 (inset) shows the polarization curves at the different points noted in the stability tests above it. The  $\text{CoO}_x/\text{NF}$  electrode exhibited





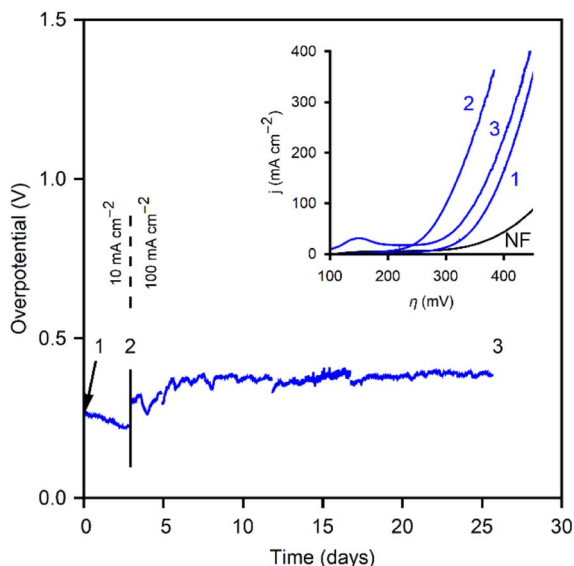


Fig. 9 CP curves of a CoNF electrode for  $10 \text{ mA cm}^{-2}$  (up to the black line) and  $100 \text{ mA cm}^{-2}$ . Numbered points where the LSVs are taken are noted. Inset: polarization curves for the bare NF and the three CoNF points noted in the CP curves.

increased performance, with a 75 mV reduction in overpotential at  $100 \text{ mA cm}^{-2}$ , reaching this current density at only 1.53 V vs. RHE ( $\eta_{100 \text{ mA cm}^{-2}} = 300 \text{ mV}$ ). This performance is impressively low overpotential for electrodes with this geometry and composition. After point “2” the current density was increased to  $100 \text{ mA cm}^{-2}$ , the usual benchmark for high-current density tests in similar studies. After 528 h of polarization the electrode was rechecked (point “3”). The polarization curve exhibited a slight decrease ( $\eta_{100 \text{ mA cm}^{-2}} = 325 \text{ mV}$ ) compared to peak performance but maintained an overall increase in performance over the initial, electrochemically-conditioned,  $\text{CoO}_x/\text{NF}$  electrode.

Fig. 9 graphically compares the OER electrocatalytic activity for the materials<sup>4,34</sup> and substrates studied in this work. This representation highlights the benefits of the method developed here, and compares the stability of the films at 10 hours of polarization vs. their initial performance. It serves to emphasize the advantages of using porous materials as electrodeposition substrates for high current densities.  $\text{CoO}_x$  films demonstrate the improvement gained moving from GC to RVC, attributable to the ten-fold increase in surface area, and to NF as an electrocatalytic material itself. Therefore, optimizing the performance based on Fig. 10 involves selecting a high surface area substrate (RVC or NF) that is electrocatalytically active (NF), followed by choosing a film that allows for high performance (to the left in the x-axis), and high stability (down in y-axis). While the benefits of using RVC and NF over GC are evident, it is important to note that bubble formation can inhibit performance at high current densities by blocking the electrochemically active surface area, thus reducing the advantages of a porous electrode over a flat one. The  $10 \text{ mA cm}^{-2}$  used as a benchmark is too low to cause this issue, but at more industrially relevant current densities ( $>100 \text{ mA cm}^{-2}$ ), the current

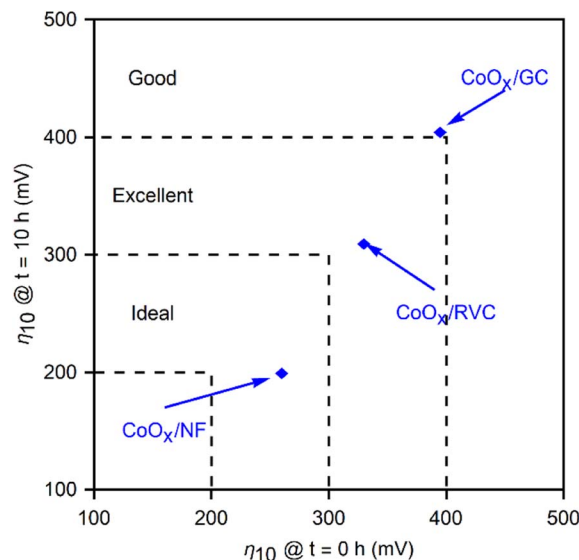


Fig. 10 Parametric plot of the overpotentials at a current density of  $10 \text{ mA cm}^{-2}$  at the start of polarization (x-axis) and at  $t = 10 \text{ h}$  (y-axis) for three  $\text{CoO}_x$  films deposited on the three substrates: GC, RVC and NF, as well as the shaded regions representing where the  $(\text{Ni/Co/FeO}_x)$  films deposited on different substrates fall. The dashed lines catalogue different activity regions into qualitative terms. All reported values are for the OER performed in 1.0 M KOH.

density ratio  $j_{\text{RVC}}/j_{\text{GC}}$  diminishes from 10 to 2. Engineering of the pore size and arrangement in the foam electrodes remains a future perspective to address these issues and lead to improved performances by making use of the full surface area at higher current densities. Nickel foam already addresses some of these issues, providing a significant contribution to the overpotential reduction due to its inherent catalytic activity for the OER and improved stability.

These results demonstrate significant advancements in the electrocatalytic performance and stability of OER catalysts, using the novel deposition method on nickel foam portrayed in our research. The porous nature of nickel foam not only allows for a high surface area but also contributes to the overpotential reduction due to its inherent catalytic activity for OER. Additionally, the simple pre-treatment of the electrode through ORR cycling serves as an effective activation method, further improving the OER performance of the films. The  $\text{CoO}_x/\text{NF}$  electrode, in particular, exhibits impressive stability and activity, outperforming the state-of-the-art catalysts of similar composition.

## Conclusions

In this study, we successfully developed an innovative cathodic electrodeposition method for amorphous thin films of metal oxides by employing the oxygen reduction reaction in dimethylformamide. The stability of superoxide radicals in the absence of metal ions, complexed by tetrabutylammonium, was probed *via* the pseudo-reversibility of the 1-electron oxygen reduction reaction on glassy carbon. Diffusion coefficients for





oxygen and  $\text{TBA}^+-\text{O}_2^{*-}$  were accurately determined using a rotating ring disk electrode.

In the presence of metals, the superoxide radical serves as the reactive species responsible for metal oxide precipitation. The highly reactive nature of this species enables rapid, oxidative deposition of any metals present near the electrode, allowing for electrodeposition without the use of complex precursors, or very low potentials. Additionally, the passivation of the electrode upon coating with thin films regarding the oxygen reduction reaction renders this method self-limiting.

Porous substrates, such as reticulated vitreous carbon and nickel foam, were coated to showcase the method's capabilities.  $\text{NiO}_x/\text{GC}$ ,  $\text{CoO}_x/\text{RVC}$ , and  $\text{CoFeNiO}_x/\text{NF}$  were further investigated and exhibited outstanding OER performance compared to similar materials. Stability differences are attributed to substrate/ $\text{MO}_x$  interactions. The long-term stability of  $\text{CoFeNiO}_x/\text{NF}$  was confirmed over 25 days at a constant polarization of  $1000 \text{ A m}^{-2}$ .

In conclusion, this novel electrodeposition method has been comprehensively explored, from understanding the underlying deposition reaction and oxygen-related kinetics, to characterizing the OER electrocatalytic performance, and evaluating the long-term stability of films coated on porous substrates.

The electrodeposition method presented in this study stands out as a groundbreaking and agenda-setting approach in the field of electrocatalysis, as it has several distinctive advantages that make it unique and outstanding compared to traditional methods in terms of versatility, simplicity, self-limiting nature, exceptional OER performance, and enhanced stability. Overall, the findings of this study provide valuable insights and offer significant advancements in the development of efficient, stable, and cost-effective OER catalysts for various energy conversion and storage applications.

## Author contributions

RP, JF, and XDB conceptualized the study, analyzed and discussed the data. RP performed experiments, acquired and processed the data. RP wrote the first draft of the manuscript. JF and XDB wrote additional parts, as well as edited and reviewed the all drafts of the manuscript. JF and XDB supervised the work. All authors discussed the results and contributed to the final manuscript.

## Conflicts of interest

There are no conflicts to declare.

## Acknowledgements

RP acknowledges VITO Strategic PhD grant funding no. 1510774. RP, JF, and XDB thank the support from the Flemish SIM MaRes programme, under grant agreement no. 150626 (Get-A-Met project). This work received funding from the European Union's Horizon Europe research and innovation programme under Grant Agreement No. 101091715 (FIREFLY project). The authors thank Omar Martinez Mora for his

support acquiring some of the electronic microscopy images, and Myrjam Mertens for her support in conducting the XRD measurements. The authors thank Maximilian König for the fruitful discussion during the revision stages of this paper.

## References

- 1 N. S. Lewis and D. G. Nocera, Powering the planet: Chemical challenges in solar energy utilization, *Proc. Natl. Acad. Sci. U. S. A.*, 2006, **103**, 15729–15735.
- 2 J. A. Turner, Sustainable hydrogen production, *Science*, 2004, **305**, 972–974.
- 3 Z. W. Seh, et al., Combining theory and experiment in electrocatalysis: Insights into materials design, *Science*, 2017, **355**, eaad4998.
- 4 C. C. McCrory, S. Jung, J. C. Peters and T. Jaramillo, Benchmarking heterogeneous electrocatalysts for the oxygen evolution reaction, *J. Am. Chem. Soc.*, 2013, **135**, 16977–16987.
- 5 T. Nakagawa, C. A. Beasley and R. W. Murray, Efficient electro-oxidation of water near its reversible potential by a mesoporous  $\text{IrO}_x$  nanoparticle film, *J. Phys. Chem. C*, 2009, **113**, 12958–12961.
- 6 M. Carmo, D. L. Fritz, J. Mergel and D. Stolten, A comprehensive review on PEM water electrolysis, *Int. J. Hydrogen Energy*, 2013, **38**, 4901–4934.
- 7 F. Song and X. Hu, Ultrathin cobalt–manganese layered double hydroxide is an efficient oxygen evolution catalyst, *J. Am. Chem. Soc.*, 2014, **136**, 16481–16484.
- 8 G. Gardner, et al., Structural basis for differing electrocatalytic water oxidation by the cubic, layered and spinel forms of lithium cobalt oxides, *Energy Environ. Sci.*, 2016, **9**, 184–192.
- 9 N. Yuan, Q. Jiang, J. Li and J. Tang, A review on non-noble metal based electrocatalysis for the oxygen evolution reaction, *Arabian J. Chem.*, 2020, **13**, 4294–4309.
- 10 L. Trotochaud, J. K. Ranney, K. N. Williams and S. W. Boettcher, Solution-cast metal oxide thin film electrocatalysts for oxygen evolution, *J. Am. Chem. Soc.*, 2012, **134**, 17253–17261.
- 11 H. Jin, et al., In situ cobalt–cobalt oxide/N-doped carbon hybrids as superior bifunctional electrocatalysts for hydrogen and oxygen evolution, *J. Am. Chem. Soc.*, 2015, **137**, 2688–2694.
- 12 Y. Liang, et al.,  $\text{Co}_3\text{O}_4$  nanocrystals on graphene as a synergistic catalyst for oxygen reduction reaction, *Nat. Mater.*, 2011, **10**, 780–786.
- 13 B. Dong, et al., Two-step synthesis of binary Ni–Fe sulfides supported on nickel foam as highly efficient electrocatalysts for the oxygen evolution reaction, *J. Mater. Chem. A*, 2016, **4**, 13499–13508.
- 14 C. G. Morales-Guio, L. Liardet and X. Hu, Oxidatively electrodeposited thin-film transition metal (oxy) hydroxides as oxygen evolution catalysts, *J. Am. Chem. Soc.*, 2016, **138**, 8946–8957.
- 15 Y. K. Kim, J. H. Kim, Y. H. Jo and J. S. Lee, Precipitating Metal Nitrate Deposition of Amorphous Metal Oxyhydroxide



- Electrodes Containing Ni, Fe, and Co for Electrocatalytic Water Oxidation, *ACS Catal.*, 2019, **9**, 9650–9662.
- 16 R. D. Smith, M. S. Prévot, R. D. Fagan, S. Trudel and C. P. Berlinguette, Water oxidation catalysis: electrocatalytic response to metal stoichiometry in amorphous metal oxide films containing iron, cobalt, and nickel, *J. Am. Chem. Soc.*, 2013, **135**, 11580–11586.
  - 17 Y. Yang, H. Fei, G. Ruan, C. Xiang and J. M. Tour, Efficient electrocatalytic oxygen evolution on amorphous nickel–cobalt binary oxide nanoporous layers, *ACS Nano*, 2014, **8**, 9518–9523.
  - 18 V. D. Silva, L. S. Ferreira, T. A. Simões, E. S. Medeiros and D. A. Macedo, 1D hollow  $\text{MFe}_2\text{O}_4$  (M = Cu, Co, Ni) fibers by Solution Blow Spinning for oxygen evolution reaction, *J. Colloid Interface Sci.*, 2019, **540**, 59–65.
  - 19 Y. Zhang, et al., Rapid synthesis of cobalt nitride nanowires: highly efficient and low-cost catalysts for oxygen evolution, *Angew. Chem., Int. Ed.*, 2016, **55**, 8670–8674.
  - 20 G. Vanhoutte, et al., Electro-precipitation via oxygen reduction: a new technique for thin film manganese oxide deposition, *J. Mater. Chem. A*, 2016, **4**, 13555–13562.
  - 21 D. R. Rolison, et al., Multifunctional 3D nanoarchitectures for energy storage and conversion, *Chem. Soc. Rev.*, 2009, **38**, 226–252.
  - 22 S. Deheryan, et al., Self-limiting electropolymerization of ultrathin, pinhole-free poly (phenylene oxide) films on carbon nanosheets, *Carbon*, 2015, **88**, 42–50.
  - 23 C. P. Rhodes, J. W. Long, M. S. Doescher, B. M. Dening and D. R. Rolison, Charge insertion into hybrid nanoarchitectures: mesoporous manganese oxide coated with ultrathin poly (phenylene oxide), *J. Non. Cryst. Solids*, 2004, **350**, 73–79.
  - 24 M. Hayyan, M. A. Hashim and I. M. AlNashef, Superoxide ion: generation and chemical implications, *Chem. Rev.*, 2016, **116**, 3029–3085.
  - 25 D. T. Sawyer, G. Chiericato, C. T. Angelis, E. J. Nanni and T. Tsuchiya, Effects of media and electrode materials on the electrochemical reduction of dioxygen, *Anal. Chem.*, 1982, **54**, 1720–1724.
  - 26 J. A. Fee and P. G. Hildenbrand, On the development of a well-defined source of superoxide ion for studies with biological systems, *FEBS Lett.*, 1974, **39**, 79–82.
  - 27 C. O. Laoire, S. Mukerjee, K. Abraham, E. J. Plichta and M. A. Hendrickson, Influence of nonaqueous solvents on the electrochemistry of oxygen in the rechargeable lithium–air battery, *J. Phys. Chem. C*, 2010, **114**, 9178–9186.
  - 28 J. D. Wadhawan, P. J. Welford, H. B. McPeak, C. E. Hahn and R. G. Compton, The simultaneous voltammetric determination and detection of oxygen and carbon dioxide: a study of the kinetics of the reaction between superoxide and carbon dioxide in non-aqueous media using membrane-free gold disc microelectrodes, *Sens. Actuators, B*, 2003, **88**, 40–52.
  - 29 D. Vasudevan and H. Wendt, Electroreduction of oxygen in aprotic media, *J. Electroanal. Chem.*, 1995, **392**, 69–74.
  - 30 C. Cui, S. Jiang and A. Tseung, Reactive Deposition of Cobalt Electrodes: VIII. Effect of Oxygen Reduction on the Deposition of Cobalt in Co (II) Chloride DMF Solution, *J. Electrochem. Soc.*, 1992, **139**, 1535.
  - 31 D. A. Corrigan and R. M. Bendert, Effect of coprecipitated metal ions on the electrochemistry of nickel hydroxide thin films: cyclic voltammetry in 1M KOH, *J. Electrochem. Soc.*, 1989, **136**, 723–728.
  - 32 M. D. Merrill and R. C. Dougherty, Metal Oxide Catalysts for the Evolution of  $\text{O}_2$  from  $\text{H}_2\text{O}$ , *J. Phys. Chem. C*, 2008, **112**, 3655–3666.
  - 33 L. Han, X. Y. Yu and X. W. Lou, Formation of prussian-blue-analog nanocages via a direct etching method and their conversion into ni-co-mixed oxide for enhanced oxygen evolution, *J. Adv. Mater.*, 2016, **28**, 4601–4605.
  - 34 M. Tahir, et al., Electrocatalytic oxygen evolution reaction for energy conversion and storage: a comprehensive review, *Nano Energy*, 2017, **37**, 136–157.
  - 35 Y. Zhao, E. A. Hernandez-Pagan, N. M. Vargas-Barbosa, J. L. Dysart and T. Mallouk, A high yield synthesis of ligand-free iridium oxide nanoparticles with high electrocatalytic activity, *J. Phys. Chem. Lett.*, 2011, **2**, 402–406.
  - 36 J. S. Sagu, D. Mehta and K. U. Wijayantha, Electrocatalytic activity of  $\text{CoFe}_2\text{O}_4$  thin films prepared by AACVD towards the oxygen evolution reaction in alkaline media, *Electrochem. Commun.*, 2018, **87**, 1–4.
  - 37 X. Liu, S. Cui, M. Qian, Z. Sun and P. Du, In situ generated highly active copper oxide catalysts for the oxygen evolution reaction at low overpotential in alkaline solutions, *Chem. Commun.*, 2016, **52**, 5546–5549.
  - 38 M. E. Lyons and M. P. Brandon, The significance of electrochemical impedance spectra recorded during active oxygen evolution for oxide covered Ni, Co and Fe electrodes in alkaline solution, *J. Electroanal. Chem.*, 2009, **631**, 62–70.
  - 39 R. L. Doyle, I. J. Godwin, M. P. Brandon and M. E. Lyons, Redox and electrochemical water splitting catalytic properties of hydrated metal oxide modified electrodes, *Phys. Chem. Chem. Phys.*, 2013, **15**, 13737–13783.
  - 40 R. L. Doyle and M. E. Lyons, An electrochemical impedance study of the oxygen evolution reaction at hydrous iron oxide in base, *Phys. Chem. Chem. Phys.*, 2013, **15**, 5224–5237.
  - 41 R. Doyle and M. Lyons, Kinetics and mechanistic aspects of the oxygen evolution reaction at hydrous iron oxide films in base, *J. Electrochem. Soc.*, 2013, **160**, H142–H154.
  - 42 J. R. Swierk, S. Klaus, L. Trotochaud, A. T. Bell and T. D. Tilley, Electrochemical study of the energetics of the oxygen evolution reaction at nickel iron (oxy) hydroxide catalysts, *J. Phys. Chem. C*, 2015, **119**, 19022–19029.
  - 43 H. Kamal, E. Elmaghraby, S. Ali and K. Abdel-Hady, Characterization of nickel oxide films deposited at different substrate temperatures using spray pyrolysis, *J. Cryst. Growth*, 2004, **262**, 424–434.
  - 44 M. S. Abouzari, F. Berkemeier, G. Schmitz and D. Wilmer, On the physical interpretation of constant phase elements, *Solid State Ionics*, 2009, **180**, 922–927.
  - 45 M. E. Lyons and M. P. Brandon, The oxygen evolution reaction on passive oxide covered transition metal



- electrodes in aqueous alkaline solution. Part 1-Nickel, *Int. J. Electrochem. Sci.*, 2008, **3**, 1386–1424.
- 46 D. M. Santos, C. A. Sequeira and J. L. Figueiredo, Hydrogen production by alkaline water electrolysis, *Quim. Nova*, 2013, **36**, 1176–1193.
- 47 J. Friedrich, C. Ponce-de-León, G. Reade and F. Walsh, Reticulated vitreous carbon as an electrode material, *J. Electroanal. Chem.*, 2004, **561**, 203–217.
- 48 W. Zhu, R. Zhang, F. Qu, A. M. Asiri and X. Sun, Design and application of foams for electrocatalysis, *ChemCatChem*, 2017, **9**, 1721–1743.

